Mapping Sea Ice Surface Topography in High Fidelity with ICESat-2

S. L. Farrell[1], K. Duncan[2], E. M. Buckley[3], J. Richter-Menge[4], R. Li[1]

[1]Department Geographical Sciences, University of Maryland, College Park, MD, USA.

[2]Earth System Science Interdisciplinary Center, University of Maryland, College Park, MD, USA.

[3]Department of Atmospheric and Oceanic Science, University of Maryland, College Park, MD, USA.

[4]Institute of Northern Engineering, University of Alaska Fairbanks, Fairbanks, AK, USA.

Corresponding author: Sinéad Louise Farrell (sineadf@umd.edu)

Key Points:

- ICESat-2 provides a new remote sensing capability to measure complex sea ice surface topography at m-scale resolution, across all seasons
- We demonstrate approaches to retrieve six, key sea ice parameters using ICESat-2 laser altimeter height measurements
- ICESat-2 observations may be used to investigate time-varying sea ice processes, advancing forecasting and modelling efforts

Abstract

The Advanced Topographic Laser Altimeter System (ATLAS) on ICESat-2 offers a new remote sensing capability to measure complex sea ice surface topography. We demonstrate the retrieval of six sea ice parameters from ICESat-2/ATLAS data: surface roughness, ridge height, ridge frequency, melt pond depth, floe size distribution and lead frequency. Our results establish that these properties can be observed in high fidelity, across broad geographic regions and ice conditions. We resolve features as narrow as 7 m, and achieve a vertical height precision of 0.01 m, representing a significant advance in resolution over previous satellite altimeters. ICESat-2 employs a year-round observation strategy spanning all seasons, across both the Arctic and Southern Oceans. Because of its higher resolution, coupled with the spatial and temporal extent of data acquisition, ICESat-2 observations may be used to investigate time-varying, dynamic and thermodynamic sea ice processes.

Plain Language Summary

The small footprint, high pulse repetition rate and six-beam configuration of the Advanced Topographic Laser Altimeter System (ATLAS) on ICESat-2 delivers the highest-fidelity measurements of sea ice surface topography ever obtained from a spaceborne platform. Since mid-October 2018, ICESat-2 has provided observations throughout the winter growth and summer melt seasons. We show that ICESat-2 measurements can be used to derive a suite of important sea ice properties, including surface roughness, pressure ridge height and frequency, lead frequency and floe size distribution in the Arctic. We also demonstrate the capability to detect individual melt ponds on multi-year sea ice, marking the first time summer melt features have been reliably detected from a space-based altimeter. ICESat-2 observations deliver unprecedented new details of several sea ice properties that will be transformational in understanding time-varying polar processes, occurring both during the winter and summer seasons, under a range of ice conditions.

1 Introduction

Observational evidence from multiple data sources demonstrates that significant, and rapid, changes are occurring in the Arctic climate system (Richter-Menge et al., 2019). As air temperatures in the Arctic warm at twice the global rate, long-term declines in sea ice extent,

age, and volume, and the duration of the winter growth period, have been observed (Perovich et al., 2019). Arctic sea ice influences global atmospheric patterns (e.g., Francis et al., 2017), oceanic thermohaline circulation, and, due to its high albedo, regulates the planetary energy balance (e.g., Curry et al., 1995). Sea ice properties (e.g., concentration, thickness, drift velocity) and processes (e.g., growth, melt, divergence, convergence) are, however, some of the most poorly-constrained variables in global climate models; neither their magnitude nor their impact on future climate projections are well understood (e.g., Turner & Comiso, 2017). High-resolution satellite measurements offer a practical solution for achieving spatially and temporally complete monitoring of sea ice in the polar oceans (Shepherd et al., 2018).

Satellite altimeters, deployed on ICESat (2003-2009) and CryoSat-2 (2010 – present), with orbital inclinations designed to observe Earth's polar regions, have delivered near-continual winter-time measurements of sea ice topography at the basin scale since 2003 (e.g. Laxon et al., 2013). These observations have revealed a decline in Arctic sea ice freeboard, thickness and volume over the last two decades (e.g. Farrell et al., 2009; Laxon et al., 2013), during which time the ice cover has transitioned from predominantly multiyear to seasonal ice (Perovich et al., 2019).

NASA's ICESat-2 continues the polar satellite altimetry record, measuring sea ice elevation to 88^{o} N/S. Since October 14, 2018, ICESat-2 has provided continual observations of both polar regions, with the exception of the 2019 summer melt season when an observational gap occurred between June 26 and July 26, 2019 due to a spacecraft anomaly. The data have been used to track the evolution of sea ice freeboard in winter (e.g., Kwok et al., 2019c). Here we present a selection of high-fidelity measurements of sea ice surface topography from ICESat-2, for a variety of Arctic sites. Our goal is to demonstrate ICESat-2's unique capability to track individual floes, from which fine-scale sea ice properties may be derived. We show examples spanning the end of winter (April 2019), through summer melt (June 2019), and fall freeze-up (September 2019). Results are validated using independent, coincident observations from airborne lidar and satellite imagery. We discuss how ICESat-2's remote sensing capabilities over sea ice will extend the utility of the data beyond fulfillment of the mission science requirement to measure freeboard (Markus et al., 2017), by enabling more-detailed process studies.

2 Data

ICESat-2 operates in a 91-day exact repeat orbit, with 1387 orbits per cycle. Over the Arctic Ocean, orbit subcycles of 4 and 29 days offer complete, basin-scale coverage. ICESat-2 carries one primary instrument, the Advanced Topographic Laser Altimeter System (ATLAS). Six ATLAS beams, arranged in three pairs, span approximately 6.6 km in the across-track direction. Beam locations are defined relative to spacecraft Reference Ground Tracks (RGTs). We use the convention *ttttccss_gtxy* to identify specific RGTs, where *t* is the RGT number, *c* is the orbit cycle, *s* is segment number, *gt* indicates "ground track", *x* is beam number and *y* indicates either left (*l*) or right (*r*) beam. Controlled pointing to the RGTs began in March 2019. Here we use the ATLAS Release 003 Level 2 ATL03 product that contains geolocated photon heights relative to the WGS84 reference ellipsoid (Neumann et al., 2020). Geolocation of individual photons results in a vertical range accuracy of 0.05 m and a precision better than 0.13 m (Brunt et al., 2019). We also use Release 002 Level 3 ATL07 sea ice surface heights (Kwok et al., 2019a), derived from ATL03.

Retrievals are validated using two independent data sets. Dedicated Operation IceBridge (OIB) under-flights of ICESat-2 were conducted in April 2019 to obtain high-resolution (2 m) Airborne Topographic Mapper (ATM) lidar data along ICESat-2 RGTs in the Canada Basin (Kwok et al., 2019b). Here we present results from April 22, 2019, when near-coincident (< ~38 minutes) ATM data were acquired. We also utilize high-resolution (10 m) visible imagery from the Sentinel-2 MultiSpectral Instrument (MSI) for validation.

3 Fine-scale Sea Ice Properties

ICESat-2's predecessor ICESat carried an analogue laser altimeter that had a large footprint (~50 m) with ~172 m spacing between shots, which limited the resolution of sea ice observations (Farrell et al., 2011). Overlapping ~12 m-diameter ICESat-2/ATLAS footprints (L. Magruder, pers. comm.), sampled every ~0.7 m along-track, offer a unique opportunity for adaptive sampling of the surface, at length scales suitable for discriminating discrete sea ice features. Following previous work using an airborne simulator for ATLAS (Farrell et al., 2015), we exploit the innovation of photon-counting laser altimetry to map the rough, topographically complex, sea ice surface at high-resolution. Prior to applying basic sea ice retracking algorithms to ATL03 photon heights, we preprocess the data to remove background noise. We do this by

retaining only photons between the 15th and 85th percentile of the per shot height distribution. ATL03 atmospheric, tidal, and geoid corrections are applied to obtain corrected elevation. Following Duncan et al. (2018) and Farrell et al. (2015), elevation is relative to the local level ice/water surface.

In the following sub-sections, we explore ICESat-2's capabilities to observe signatures of both sea ice dynamics (ice pack convergence and divergence) and thermodynamics (sea ice melt/freeze). We include a brief description of the retrieval of six sea ice parameters from ATL03 data: surface roughness, ridge height, ridge frequency, melt pond depth, floe size distribution and lead frequency. We then discuss (in Section 4) their utility in sea ice process studies.

3.1 Surface roughness and pressure ridges

Sea ice roughness (σ_h) provides an indication of both the mechanical deformation history of the ice cover and snow distribution across the surface. It is also a proxy for ice thickness. Knowledge of σ_h is required to understand the exchange of turbulent energy between the ice and atmosphere, and drag-induced ice dynamics (Zwally et al., 2003). Here, σ_h is the standard deviation of ATL07 surface height within 25 km-long segments. To illustrate ICESat-2's capability for obtaining σ_h we consider the Arctic Ocean as a whole (Figure 1a), but also highlight two regions of the ice cover (regions A and B, Figure 1a) with distinct roughness characteristics. In April 2019, Arctic-wide σ_h averaged 0.18 m (Figure 1b) but showed a spatial pattern consistent with the known geographic locations of the seasonal ice zone and the more heavily-deformed multiyear ice cover (Fig. 3 in Perovich et al., 2019). Region A, north of Borden Island (Figure 1a, spanning 79.5°-83°N, 100°-120°W), contained multiyear ice ≥ 3 years old and had an average σ_h of 0.3 m, while region B (Figure 1a, spanning 76.25°-81°N, 140°-160°W), an area of seasonal ice in the Beaufort Gyre, was half as rough (σ_h = 0.15 m, Figure 1b).

Focusing on representative, 1 km-long segments within each region, we apply the University of Maryland-Ridge Detection Algorithm (UMD-RDA) to the preprocessed (Section 3) ATL03 photon heights. The UMD-RDA retains the 99th percentile of the photon height distribution for a 5-shot aggregate, applied on a per-shot basis so as to retain full along-track resolution (0.7 m). When applied to ICESat-2 retrievals over sea ice we obtain a surface

elevation profile from which individual pressure ridges may be detected. Following previous studies (e.g., Duncan et al., 2018) we define a pressure ridge sail as any local maxima occurring above 0.6 m. This threshold distinguishes ridges from lower-amplitude surface features (e.g., snow dunes or sastrugi). Local minima lying above the threshold height are also flagged. Ridge width is the along-track distance between minima, or the point(/s) at which elevation drops below the threshold height, whichever is closer to the local maxima. Maxima separated by ≤ 10 m are not considered unique and are instead counted as a single ridge (e.g. ridge 8, Figure 1c).

Results from the UMD-RDA reveal an average sail height (h_s) of 1.5 m for 9 ridges spanning 10.7 – 51.8 m in width in region A (Figure 1c). Coincident OIB ATM elevations show h_s averaged 1.6 m, verifying the ICESat-2 UMD-RDA result. The altimeter height comparison, as well as insight from OIB imagery (Figure 1d), confirms both the location and number (n_r) of distinct ridges. The ATL07 surface height algorithm accurately detects individual deformation features in this region of multiyear ice, however h_s is underestimated by 0.4 m (0.3 m) when compared with ATM (UMD-RDA) (Figure 1c). The results from region A contrast with the UMD-RDA statistics obtained over the smoother surface topography of region B. Here, h_s averaged 0.8 m for n_r = 5, ranging 7.1 – 35.7 m in width (Figure 1e). In this area the ATL07 dataset performs poorly, enabling the detection of only one ridge, with h_s = 0.61 m, suggesting surface roughness on seasonal ice may be underestimated by the ATL07 algorithm.

Regions A and B contain approximately the same number of 1-km segments (n_{seg}, Figure 1f), derived from between 64 and 78 RGTs in April 2019. Aggregating these measurements illustrates distinctions in the number of ridges (n_r) and their frequency (f_r, Figure 1f), and in h_s (Figure 1g), as a function of ice type. The rougher, older ice in region A was more heavily deformed than the ice in region B, with ~ 2.5 times more ridges, that were, on average, 0.28 m (0.25 m) taller in mean (modal) h_s. We found that the 99th percentile of sail height ($h_{s\,99}$) was 0.67 m larger in region A than in region B. These results are consistent with an earlier study (Duncan et al., 2020) that found $h_{s\,99}$ is a strong indicator of the predominant ice type in which a pressure ridge forms.

3.2 Melt ponds

Following the end of winter, as air temperatures warm, both thermodynamic and dynamic processes introduce meltwater to the system. The presence of low-albedo ponds on the sea ice

surface enhances the ice-albedo feedback by increasing absorption of shortwave radiation, altering Earth's energy budget (Curry et al., 1995). The detection of melt ponds with spaceborne sensors has proved challenging since ponds are radiometrically similar to open water/leads and cover small areas (~5 – 100 m^2, Perovich et al., 2002). Early ICESat-2 observations demonstrated an unexpected capability to penetrate shallow, low turbidity water to measure coastal bathymetry and identify glacial melt ponds on Antarctic ice shelves (Magruder et al., 2019; Parrish et al., 2019). These early results, coupled with ICESat-2's high resolution, suggest the possibility of measuring sea ice melt pond depth and motivate the following analysis.

We examine ten, 1 km-long ATL03 segments (Figure 2a, gray dots) acquired along RGTs crossing the Lincoln Sea (region C, Figure 1a) during the period June 17-22, 2019. Ice in this region was very rough (Figure 1a) and comprised mainly multiyear floes ≥ 3.5 m thick (Fig. 5 in Perovich et al., 2019). The evolution of melt in the Lincoln Sea in 2019 was consistent with field observations (e.g., Perovich & Polashenski, 2012). The Sentinel-2 MSI time series for the region (not shown) confirms that surface snow melt was underway by 28 May, and pond coverage was widespread by 13 June accompanied by a significant drop in surface albedo. Sentinel-2 imagery of the region on June 22, 2019 (Figure 2b), acquired 37 minutes prior to ICESat-2 RGT 13070304, confirms the presence of melt ponds on the sea ice surface.

Following Buckley et al. (2020), we classified open water, ponded surfaces, and ice floes in the Sentinel-2 scene (Figure 2b) and used this to validate the presence of ponds in the ICESat-2 data. By tracking the movement of 10 floes between two overlapping Sentinel-2 images acquired 50 minutes apart (not shown), we estimated an average ice drift rate of 9.3 cms^{-1}. To account for the time elapsed between the Senitnel-2 and ICESat-2 acquisitions, we applied a drift correction of 206 m to the imagery. This provided the exact geolocation of melt features in the Sentinel-2 scene at the time of the ICESat-2 overpass. Assessment of the ICESat-2 segments (Figure 2a) reveals strong surface returns from the approximately level sea ice surface and classic concave pond features (Perovich et al., 2003). The latter are a result of ICESat-2 returns from melt pond bottoms (MP1-10, Figure 2a). Four ponds (MP7-10) can be identified in both the Sentinel-2 (Figure 2b, insets) and ICESat-2 data (Figure 2a).

The small-scale pond features, ranging ~60 - 280 m wide (Figure 2a), are not captured by higher-level ICESat-2 products, such as ATL07 (Figure 2a, cyan). Hence, we developed the

University of Maryland-Melt Pond Algorithm (UMD-MPA) to identify pond surfaces (Figure 2a, black) and bathymetry (Figure 2a, magenta) in the ATL03 data. To determine pond depth (h_{mp}), the algorithm utilizes a two-dimensional histogram with 10 m along-track and 0.1 m vertical resolution. Pond surface elevation is defined by the mode closest to mean segment elevation. Ponds occur where a secondary mode in the elevation distribution exists below the surface mode (e.g. see MP2, Figure 2a). The leading edge of the secondary mode defines pond bathymetry since this represents the first photon returns from the pond bottom. Its selection mitigates the impact of photons with delayed arrival times at the detector. Initially, h_{mp} is derived by subtracting bottom elevations from pond surface elevation. We note, however, that photon heights for photons returned from within ponds are not inherently corrected for the refraction of light at the air-water interface. Therefore, following Parrish et al. (2019, and references therein), we apply a refraction correction wherein estimated pond depth is scaled by 0.749, the ratio of the refractive index of air (1.00029) to water (1.33567). After correcting for refraction and linearly interpolating at 5 m along-track resolution, the h_{mp} distribution for MP1-10 indicates that h_{mp} ranged 0.04 – 2.4 m, with a modal (mean) depth of 0.35 m (0.80 m) (Figure 2c). 75% of the h_{mp} retrievals were ≤ 1.1 m. MP9 (inset, Figure 2b), an approximately circular pond, is likely younger than the other geometrically more complex ponds (Perovich et al., 2002). Combining maximum h_{mp} (1.73 m, Figure 2a) with Sentinel-2 pond area (37,000 m^2, Figure 2b), and assuming pond volume is approximated by the volume of a spherical cap, we estimate that MP9 contains ~32,000 m^3 of melt water.

The ICESat-2-derived estimates of maximum h_{mp} are deeper than those typically observed in the field (e.g., Perovich et al., 2003). Pond depths can, however, be explained by their geographical setting on rough multiyear ice and the atmospheric conditions under which the ponds formed. Regional temperatures in May 2019 were ~4-6 ^{o}C above average (Vose et al., 2014) allowing for enhanced snow melt and mature pond evolution. Sophisticated simulations of pond evolution (Scott & Feltham, 2010) have suggested that rapid pond deepening, of over 0.5 m

in 10 days, can occur on thick, rough multiyear ice, with mean pond depth reaching 0.85 m, in line with the observations shown here.

3.3 Floe size distribution and lead frequency

As the melt season progresses mechanical breakup continues and the unconsolidated ice pack comprises discrete floes in free drift. Open water fraction increases rapidly, amplified by lateral melt, and floe size decreases. Solar heat input to the upper ocean increases, further enhancing melt (Perovich & Richter-Menge, 2015). Lead and floe size statistics, and their temporal and regional variability, are needed to understand ice-ocean-atmosphere heat fluxes in summer. Previously, satellite altimeters faced challenges observing summer ice processes. ICESat operated in campaign mode and did not obtain summer data (Farrell et al., 2009), while CryoSat-2 has limited along-track resolution (~300 m) and cannot distinguish between summer melt features (ponds and leads) on the basis of radar altimeter return power, since the radar backscatter coefficient of sea ice is sensitive to meltwater (Wingham et al., 2006).

Here, we revisit the ice cover at the onset of fall freeze-up, focusing on ICESat-2 observations in the Canada Basin (region D, Figure 1a) in early September. Floes in the region range 10s to 10,000s meters wide (Figure 3a) and are surrounded by thin nilas (WMO, 1970). Applying the UMD-RDA to a 200 km-long ICESat-2 transect we obtain surface elevation profiles for the three strong beams. Aggregating heights from ten short (~1 km-long) segments at locations along the beams (cyan diamonds, Figure 3a) we obtain a zero-mean elevation distribution with a standard deviation of 0.009 m (blue curve, Figure 3b), illustrating the vertical height precision of ATLAS over leads. This is a 50% improvement in capability compared with ICESat, which had a demonstrated precision of ~0.02 m over leads (Kwok et al., 2004). We note that while the major mode of the ATL07 height distribution for the same leads is consistent with the UMD-RDA results (gray curve, Figure 3b), 23% of the data fall into a secondary mode, with a mean elevation of 0.05 m. The reason for this secondary mode is currently unknown, but its impact is a positive bias in ATL07 sea surface heights.

To demonstrate ICESat-2's ability to discriminate individual floes we examine a shorter (~7.5 km) representative area. In this region, we compare ICESat-2 elevations with a coincident Sentinel-2 image acquired just 11 minutes after the ICESat-2 pass (Figure 3c). The imagery reveals nilas between floes of varying sizes, with some evidence of finger rafting. The ICESat-2

lead/floe locations, and deviations in their elevation, accurately correspond with the local ice conditions revealed in the Sentinel-2 MSI data. The ICESat-2 retrievals demonstrate level elevations across the refrozen lead surfaces and floes ranging 20 m to 3.034 km wide. ICESat-2 modal freeboard, computed at the floe scale, ranged 0.05 m to 1.35 m (Figure 3c). If we suppose that the floes are in hydrostatic equilibrium with an ice density of 880 kgm^{-3} and that a thin (~0.05 m), low density (~220 kgm^{-3}) dusting of snow has accumulated on these floes, we can estimate an average ice thickness of 2.85 m, which is reasonable when compared with ice mass balance estimates (Perovich & Richter-Menge, 2015).

We extend the analysis to ~600 km by combining ICESat-2 retrievals from the three strong beams and compute lead and floe statistics. Because of the orientation of the track with respect to the floes (Figure 3a), we do not strictly measure lead width or floe diameter. But, due to >600 km sample size, the statistics are regionally and seasonally representative. Classifying open water and ice floes in the Sentinel-2 scene (following Buckley et al., 2020), we tagged lead and floe pixels along the ICESat-2 track and used these for validation. Based on the results in Figure 3b, leads are identified in the ICESat-2 data as level ice surfaces with ≥ 15 contiguous retrievals (~10 m along-track width) within 0.1 m of local sea level with a standard deviation of ≤ 0.01 m. Lead retrievals accounted for 27.6 % of the ICESat-2 data, which is consistent with a regional open water fraction of 25.1% derived from Sentinel-2. ICESat-2 retrievals indicate 0-2 distinct leads per kilometer, with an average lead frequency of 1.3 km^{-1}, in close agreement with Sentinel-2 (Figure 3d). While leads ranged 10 m to > 3 km, average (median) lead width was 235 m (71 m), and 75% of leads were <200 m wide (Figure 3e). Floes, on the other hand, averaged 479 m and 75% were <600 m wide (Figure 3f). Floe and lead widths differed by 0-14 m between the two independent estimates (Figures 3e, 3f), demonstrating the quality of the altimeter-derived metrics. Moreover, the ICESat-2 statistics are consistent with recent studies wherein high-resolution optical and SAR imagery revealed summer ice floe diameters ranging 10s to 1000s meters, and averaging <200 m wide (Arntsen et al., 2015; Hwang et al., 2017).

4 Discussion

The evidence provided here establishes that the small footprint and high pulse repetition frequency (10 kHz) of ATLAS on ICESat-2 is capable of resolving individual floes, sails and ponds on the sea ice cover. ICESat-2 retrievals deliver unprecedented quality in the measurement

of sea ice properties including floe size distribution, lead frequency, and sail height and frequency. They also offer the new capability to measure sea ice melt pond depth, derived from pond bathymetry, the first such measurements to be retrieved using spaceborne altimetry. We have shown that sea ice surface features as narrow as 7.1 m may be detected. ICESat-2's capability to retrieve fine-scale sea ice properties year-round will be transformational in understanding time-varying sea ice processes, and will advance interpretation of lower-resolution remote sensing data. Evaluating the skill of sea ice process models has been heretofore hindered by a lack of high-resolution observations covering large spatial and temporal scales (Roach et al., 2018). The ICESat-2 observation strategy will also address this need.

By applying customized surface re-tracking algorithms to ATL03 photon heights we captured signatures of dynamic ice convergence (pressure ridges) and divergence (leads), and evidence of summer melt (a thermodynamic process). Our examples show that over level surfaces, such as recently refrozen leads, an elevation precision of 0.01 m can be achieved, representing a considerable advance over ICESat. Discrimination of leads, and accurate measurement of their height, is critical for remote retrieval of sea ice freeboard and thickness using altimeter techniques, because lead elevation approximates local sea surface height and thus provides a reference level from which freeboard can be derived (Farrell et al., 2009). Here we have demonstrated that floe-scale freeboard may be retrieved with ICESat-2. Statistical analysis of individual floes, and their freeboard, will inform algorithm development for current and future satellite altimeter missions. Furthermore, the joint sea ice floe size thickness distribution (FSTD) is required to understand the impact of a geometrical sampling error, an error of omission in lower-resolution radar altimeter retrievals (Envisat, CryoSat-2) over sea ice (Wingham et al., 2006). Quantifying this error is critical when combining estimates of sea ice thickness from multiple altimetric sensors with varying resolutions.

High-resolution observations from ICESat-2, such as those shown here, will fill a gap in knowledge required to advance sea ice modelling (Horvat & Tziperman, 2017). For example, ICESat-2 measurements of ice pack growth in winter compliment those obtained by CryoSat-2 and will enable investigations of both dynamic and thermodynamic thickening. Routine retrieval of surface roughness, lead frequency and the FSTD will help advance drag-parameterization in the next generation of sea ice models. Observing sea ice evolution during summer melt and fall freeze-up will also improve our understanding of thermodynamically-driven mass loss (Perovich

& Richter-Menge, 2015). Extending the present analysis of melt ponds to determine regional variability in pond depth and volume, and their temporal evolution, will be useful for assessing current parameterizations in melt pond models (Hunke et al., 2013). We note that the spatial coverage of Sentinel-2 images across the Arctic Ocean (limited by orbit inclination, cloud interference, and crossover timing with ICESat-2) restricts the extension of the present approach to estimate pond volume at the Arctic Ocean scale. The potential exists however to estimate surface topography, melt pond depth and ice thickness simultaneously, with ICESat-2 data alone. This may be helpful in further constraining our understanding of ice albedo evolution during summer (Eicken et al., 2004). Tracking both dynamic and thermodynamic processes with ICESat-2, across a more comprehensive range of sea ice conditions, and seasons, than was heretofore possible with remote sensing techniques, will also permit examination of ice-ocean-atmosphere exchanges of energy, mass and momentum, supporting improved understanding of the connections between sea ice variability and climate forcings.

Acknowledgments

This study is supported under NASA Cryosphere Program Grants NNX15AE14G and 80NSSC17K0006. We thank the ICESat-2 science team and project science office for processing data used in this study, and J. M. Kuhn for assistance with altimetry data processing techniques. ICESat-2 data are available online from NSIDC (https://nsidc.org/data/icesat-2). ATM data are available at (https://nsidc.org/data/ilatm1b). Sentinel-2 MSI imagery are available at: https://scihub.copernicus.eu/dhus/#/home. Temperature data available from NOAA/ESRL Physical Sciences Laboratory at https://www.psd.noaa.gov/.

Figures

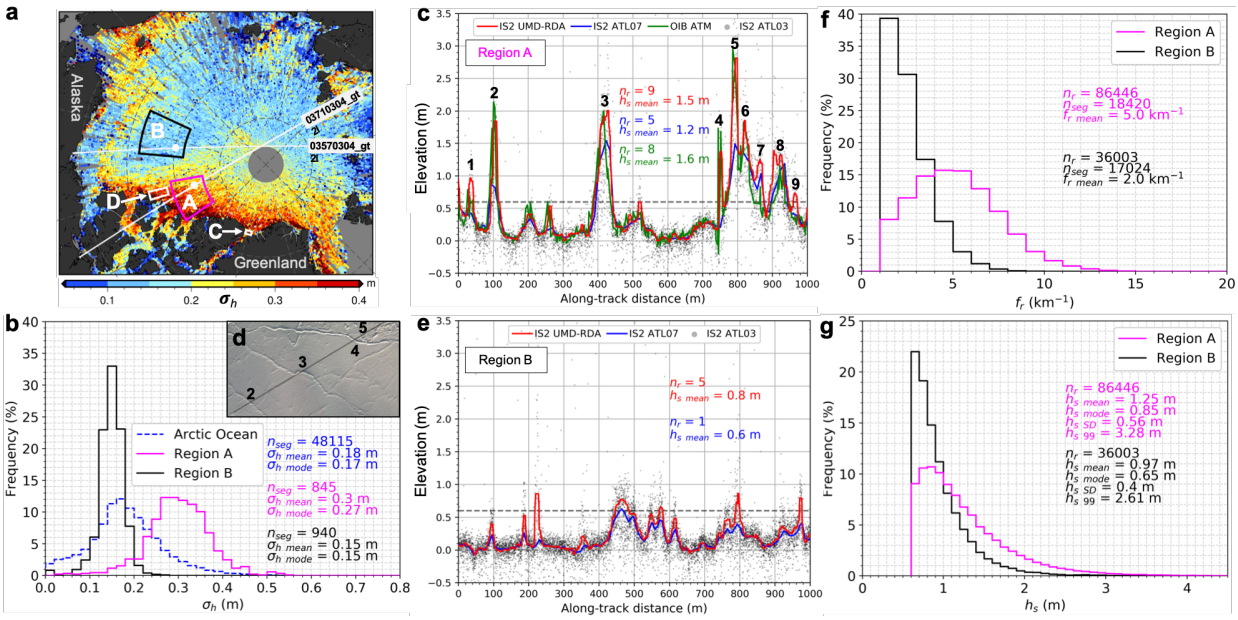

Figure 1. Arctic sea ice roughness and pressure ridge characteristics prior to melt. (a) Ice surface roughness (σ_h) in April 2019 derived from ICESat-2 ATL07, mapped at 1/8°. Regions marked A-D are sites of detailed analyses described in the text. (b) Distributions of σ_h for the Arctic Ocean (blue dashed line) and regions A (magenta line) and B (black line), as outlined in (a). (c) 1 km-long transect of sea ice elevation within region A (at white dot) on 22 April, 2019, derived from the UMD-RDA (red line), ATL07 (blue line) and ATL03 (gray dots) ICESat-2 products, and OIB ATM lidar data (green line). Distinct ridge sails are numbered. (d) Coincident OIB image of Region A transect, where numbered features correspond to sails detected in (c). (e) Same as in (c) but for transect in region B (at white dot). Note, coincident OIB data were not acquired for this transect. (f) Ridge frequency (f_r) in regions A (magenta line) and B (black line). (g) Same as in (f) but for sail height (h_s).

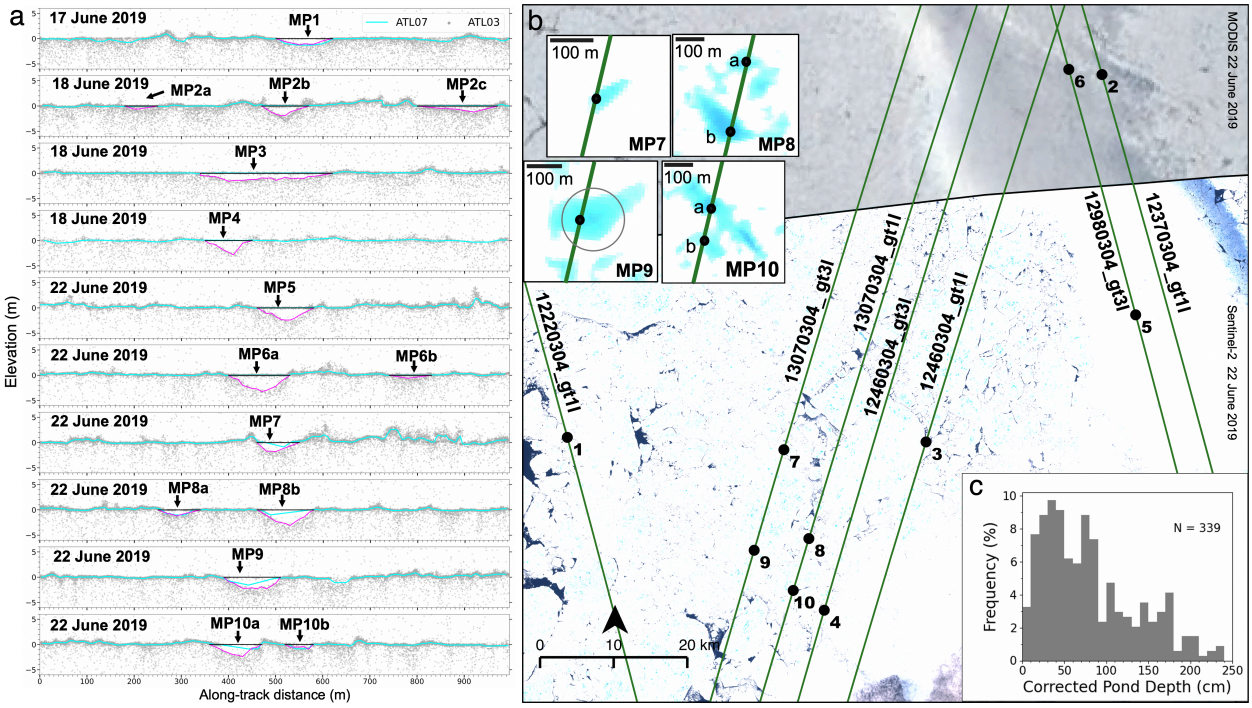

Figure 2. Detection of sea ice melt ponds with ICESat-2. (a) ATL03 photon heights (gray), ATL07 surface height (cyan), and UMD-MPA-derived melt pond (MP) surface (black) and bottom (magenta) elevations. (b) Validation of melt signals in a coincident Sentinel-2 MSI image collected June 22, 2019 at 19:50:26 UTC, 37 minutes prior to the ICESat-2 overpass on RGT 13070304. (c) Depth distribution for ponds MP1-10 shown in (a).

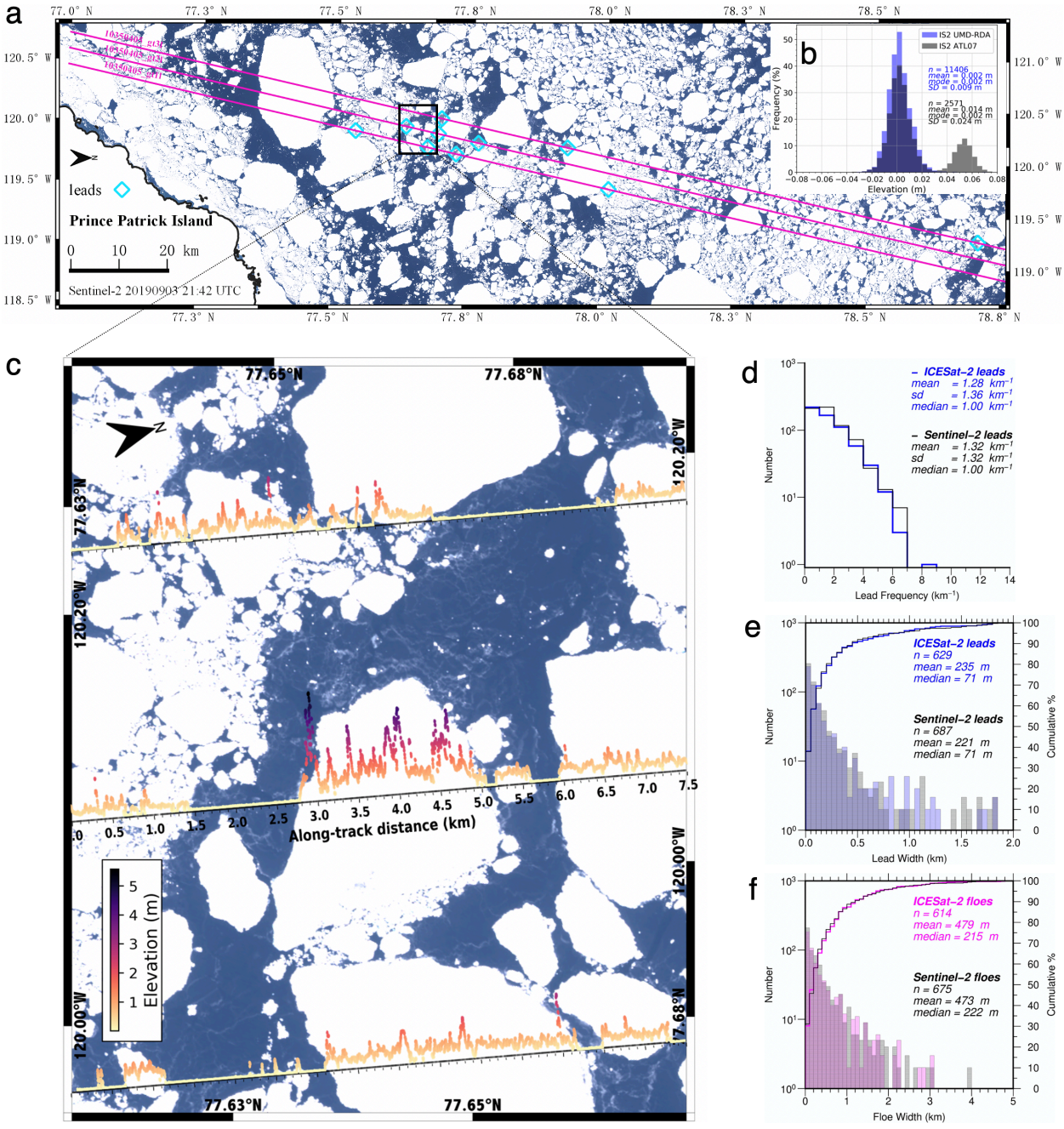

Figure 3. Arctic floe size distribution and lead frequency at the end of summer. (a) Sea ice conditions in the Canada Basin (region D, figure 1) on September 3, 2019 as observed by Sentinel-2. Coincident data obtained along a ~200 km-long ICESat-2 transect (magenta lines). (b) Elevation derived from the UMD-RDA (blue) and ATL07 (gray) ICESat-2 products over ten leads (cyan diamonds, a). (c) 7.5 km-long transect of sea ice elevation within highlighted region (black box, a), derived from the UMD-RDA ICESat-2 product, overlaid on a coincident Sentinel-2 MSI image. Elapsed time between satellite acquisitions was 11 minutes. (d) Lead frequency

370 derived from ICESat-2 (blue) and Sentinel-2 (black) along the three strong beams of
371 RGT10350405 shown in (a). (e) Lead width statistics derived from ICESat-2 (blue) and Sentinel-
372 2 (black). (f) Floe size statistics derived from ICESat-2 (magenta) and Sentinel-2 (black).

373

374 **References**

375

376 Arntsen A. E., Song A. J., Perovich D. K. & Richter-Menge J. A. (2015). Observations of the
377 summer breakup of an Arctic sea ice cover. *Geophys Res Lett*, *42*, 8057–
378 8063, http://dx.doi.org/10.1002/2015GL065224

379

380 Brunt, K. M., Neumann, T. A., & Smith, B. E. (2019). Assessment of ICESat-2 ice sheet surface
381 heights, based on comparisons over the interior of the Antarctic ice sheet. *Geophysical Research*
382 *Letters*, *46*, 13,072–13,078. https://doi.org/10.1029/2019GL084886

383

384 Buckley, E. M., Farrell, S. L., Duncan, K., Connor, L. N., Kuhn, J. M., & Dominguez, R. T.
385 (2020). Classification of sea ice summer melt features in high-resolution IceBridge imagery. *J.*
386 *Geophys. Res*., *125*, e2019JC015738. https://doi.org/10.1029/2019JC015738

387

388 Curry, J. A., Schramm, J. L., & Ebert, E. E. (1995). Sea ice-albedo climate feedback mechanism.
389 *Journal of Climate*, *8*(2), 240-247.

390

391 Duncan, K., Farrell, S. L., Connor, L. N., Richter-Menge, J. & Dominguez, R. (2018). High-
392 Resolution Airborne Observations of Sea Ice Pressure-Ridge Sail Height. *Annals of Glaciology*,
393 *59*(76pt2), 137-147. https://doi.org/10.1017/aog.2018.2

394

395 Duncan, K., Farrell, S. L., Hutchings, J., & Richter-Menge, J. (2020). Late Winter Observations
396 of Sea Ice Pressure Ridge Sail Height. *IEEE Geoscience & Remote Sensing Lett*.
397 https://doi.org/10.1109/LGRS.2020.3004724

398

399 Eicken, H., Grenfell, T. C., Perovich, D. K., Richter-Menge, J. A. & Frey, K. (2004). Hydraulic
400 controls of summer Arctic pack ice albedo. *J. Geophys. Res.*, *109*, C08007.
401 https://doi.org/10.1029/2003JC001989
402
403 Farrell, S. L., Brunt, K. M., Ruth, J. M., Kuhn, J. M., Connor, L. N., & Walsh, K. M. (2015). Sea
404 Ice Freeboard Retrieval using Digital Photon-counting Laser Altimetry. *Ann. Glaciol.*, *56*(69),
405 167–174. https://doi.org/10.3189/2015AoG69A686
406
407 Farrell, S. L., Laxon, S. W., McAdoo, D. C., Yi, D., & Zwally, H. J. (2009). Five years of Arctic
408 sea ice freeboard measurements from the Ice, Cloud and land elevation Satellite. *J. Geophys.*
409 *Res.*, *114*, C04008. https://doi.org/10.1029/2008JC005074
410
411 Farrell, S. L., Markus, T., Kwok, R. & Connor, L. (2011). Laser Altimetry Sampling Strategies
412 over Sea Ice. *Annals Glaciol.*, *52*(57), 69-76. https://doi.org/10.3189/172756411795931660
413
414 Horvat, C., & Tziperman, E. (2017). The evolution of scaling laws in the sea ice floe size
415 distribution. *J. Geophys. Res. Oceans*, *122*, 7630–7650. https://doi.org/10.1002/2016JC012573
416
417 Hunke, E. C., Hebert, D. A., & Lecomte, O. (2013). Level-ice melt ponds in the Los Alamos sea
418 ice model, CICE. *Ocean Modelling*, *71*, 26-42.
419
420 Hwang, B., Ren, J., McCormack, S., Berry, C., Ayed, I. B., Graber, H. C., & Aptoula, E. (2017).
421 A practical algorithm for the retrieval of floe size distribution of Arctic sea ice from high-
422 resolution satellite Synthetic Aperture Radar imagery. *Elem Sci Anth*, *5*.
423
424 Kwok, R., G. Cunningham, T. Markus, D. Hancock, J. H. Morison, S. P. Palm, S. L. Farrell, A.
425 Ivanoff, J. Wimert, & the ICESat-2 Science Team. (2019a). ATLAS/ICESat-2 L3A Sea Ice
426 Height, Version 2. Boulder, Colorado USA. NSIDC: National Snow and Ice Data Center.
427 https://doi.org/10.5067/ATLAS/ATL07.002
428

Kwok, R., Kacimi, S., Markus, T., Kurtz, N. T., Studinger, M., Sonntag, J. G., et al. (2019b). ICESat-2 surface height and sea ice freeboard assessed with ATM lidar acquisitions from Operation IceBridge. *Geophysical Research Letters*, *46*. https://doi.org/10.1029/2019GL084976

Kwok, R., Markus, T., Kurtz, N. T., Petty, A. A., Neumann, T. A., Farrell, S. L., Cunningham, G. F., Hancock, D. W., Ivanoff, A., & Wimert, J. (2019c), Surface height and sea ice freeboard of the Arctic Ocean from ICESat-2: Characteristics and early results. *J. Geophys. Res*., *124*. https://doi.org/10.1029/2019JC015486

Kwok, R., Zwally, H. J., & Yi, D. (2004). ICESat observations of Arctic sea ice: A first look. *Geophys. Res. Lett.*, *31*, L16401. https://doi.org/10.1029/2004GL020309

Laxon, S. W., Giles, K. A., Ridout, A. L., Wingham, D. J., Willatt, R., Cullen, R., Kwok, R., Schweiger, A., Zhang, J., Haas, C., Hendricks, S., Krishfield, R., Kurtz, N., Farrell, S. L., & Davidson, M. (2013). CryoSat Estimates of Arctic Sea Ice Volume. *Geophys. Res. Lett.*, *40*(4), 732-737. https://doi.org/10.1002/grl.50193

Magruder, L., Neumann, T., Fricker, H., Farrell, S., Brunt, K., Gardner, A., ... & Kurtz, N. (2019). New Earth orbiter provides a sharper look at a changing planet. *Eos*, *Transactions American Geophysical Union*, *100*. https://doi.org/10.1029/2019EO133233

Markus, T., Neumann, T., Martino, A., Abdalati, W., Brunt, K., Csatho, B., Farrell, S. et al. (2017). The Ice, Cloud, and land Elevation Satellite-2 (ICESat-2): Science requirements, concept, and implementation. *Rem. Sens. Environ*., *190*, 260-273. https://doi.org/10.1016/j.rse.2016.12.029

Neumann, T. A., A. Brenner, D. Hancock, J. Robbins, J. Saba, K. Harbeck, A. Gibbons, J. Lee, S. B. Luthcke, T. Rebold, et al. (2020). ATLAS/ICESat-2 L2A Global Geolocated Photon Data, Version 3. Boulder, Colorado USA. NSIDC: National Snow and Ice Data Center. https://doi.org/10.5067/ATLAS/ATL03.003

460 Parrish, C. E., Magruder, L. A., Neuenschwander, A. L., Forfinski-Sarkozi, N., Alonzo, M., &
461 Jasinski, M. (2019). Validation of ICESat-2 ATLAS Bathymetry and Analysis of ATLAS's
462 Bathymetric Mapping Performance. *Remote Sensing*, *11*(14), 1634.
463
464 Perovich, D. K., Grenfell, T.C., Richter-Menge, J. A., Light, B., Tucker III, W. B., & Eicken, H.
465 (2003). Thin and thinner: Sea ice mass balance measurements during SHEBA. *J. Geophys. Res.*,
466 *108*(C3), 8050. https://doi.org/10.1029/2001JC001079
467
468 Perovich, D., Meier, W., Tschudi, M., Farrell, S., Hendricks, S., Gerland, S., Kaleschke, L.,
469 Ricker, R., Tian-Kunze, X., Webster, M., & Wood, K. (2019). Sea ice. In *Arctic Report Card*
470 *2019*, J. Richter-Menge, M. L. Druckenmiller, and M. Jeffries (Eds.).
471 http://www.arctic.noaa.gov/Report-Card
472
473 Perovich, D. K., & Polashenski, C. (2012). Albedo evolution of seasonal Arctic sea ice.
474 *Geophys. Res. Lett.*, *39*, L08501. https://doi.org/10.1029/2012GL051432
475
476 Perovich, D. K., & Richter-Menge, J. A. (2015). Regional variability in sea ice melt in a
477 changing Arctic. *Phil. Trans. R. Soc. A, 373*, 20140165. http://doi.org/10.1098/rsta.2014.0165
478
479 Perovich, D. K., Tucker III, W. B., & Ligett, K. A. (2002). Aerial observations of the evolution
480 of ice surface conditions during summer. *J. Geophys. Res*., *107*(C10), 8048.
481 https://doi.org/10.1029/2000JC000449
482
483 Roach, L. A., Horvat, C., Dean, S. M., & Bitz, C. M. (2018). An emergent sea ice floe size
484 distribution in a global coupled ocean-sea ice model. *Journal of Geophysical Research: Oceans*,
485 *123*, 4322–4337. https://doi.org/10.1029/ 2017JC013692
486
487 Richter-Menge, J., Osborne, E., Druckenmiller, M., & Jeffries, M. O. (Eds.). (2019). The Arctic.
488 In *State of the Climate in 2018*, *Bull. Amer. Meteor. Soc.*, *100* (9), S141–S168.
489 https://doi.org/10.1175/2019BAMSStateoftheClimate.1
490

491 Scott, F., & Feltham, D. L. (2010). A model of the three-dimensional evolution of Arctic melt
492 ponds on first-year and multiyear sea ice. *J. Geophys. Res.*, *115*, C12064,
493 https://doi.org/10.1029/2010JC006156
494
495 Shepherd, A., Fricker, H. A., & Farrell, S. L. (2018). Trends and Connections Across the
496 Antarctic Cryosphere. *Nature*, *558*, 223-232, https://doi.org/10.1038/s41586-018-0171-6
497
498 Turner, J. & Comiso, J. (2017). Solve Antarctica's sea-ice puzzle. *Nature*, *547*(7663), 275-277.
499
500 Vose, R.S., Applequist, S., Durre, I., Menne, M.J., Williams, C.N., Fenimore, C., Gleason, K. &
501 Arndt, D. (2014). Improved Historical Temperature and Precipitation Time Series For U.S.
502 Climate Divisions. *Journal of Applied Meteorology and Climatology*.
503 http://dx.doi.org/10.1175/JAMC-D-13-0248.1
504
505 Wingham, D. J., Francis, C. R., Baker, S., Bouzinac, C., Brockley, D., Cullen, R., de Chateau-
506 Thierry, P., Laxon, S. W., Mallow, U., Mavrocordatos, C. and Phalippou, L. (2006). CryoSat: A
507 mission to determine the fluctuations in Earth's land and marine ice fields. *Advances in Space*
508 *Research*, *37*(4), 841-871. http://dx.doi.org/10.1016/j.asr.2005.07.027
509
510 World Meteorological Organization. (1970). Sea ice nomenclature: Terminology, Codes and
511 Illustrated Glossary, WMO/OMM/ BMO 259, TP 145, World Meteorological Organization,
512 Geneva.
513 https://www.jcomm.info/components/com_oe/oe.php?task=download&id=27226&version=Marc
514 h 2014&lang=1&format=1
515
516 Zwally, H. J., Schutz, B., Abdalati, W., Abshire, J., Bentley, C., Brenner, A., ... & Herring, T.
517 (2002). ICESat's laser measurements of polar ice, atmosphere, ocean, and land. *Journal of*
518 *Geodynamics*, *34*(3-4), 405-445.
519